Rheologica Acta (2018) 57:15–27
https://doi.org/10.1007/s00397-017-1058-4

ORIGINAL CONTRIBUTION

Stress decomposition analysis in hard and soft sphere suspensions: double peaks in the elastic stress of hard sphere suspensions and its characteristic and structural origin

Chan Hyung Park[1] · Kyung Hyun Ahn[1] · Seung Jong Lee[1]

Received: 28 March 2017 / Revised: 13 November 2017 / Accepted: 13 November 2017 / Published online: 21 November 2017

Abstract
Brownian dynamics simulations under large amplitude oscillatory shear flow at an intermediate volume fraction in both hard and soft sphere systems have been carried out. Elastic and viscous stresses for the two systems are calculated by using the stress decomposition method. Careful investigation of "double peaks," which are experimentally observed only in the elastic stress of hard sphere systems, has been conducted. When comparing hard and soft sphere systems in simulation, double peaks are observed only in hard sphere systems, within a specific strain amplitude range. The structures of hard sphere systems at different strain amplitudes, where double peaks appear and not, are compared. Excess entropy concept is adopted to evaluate the extent of particle alignment during the cycle. According to the structural analyses, double peaks are created when the structural difference between maximum-ordered and minimum-ordered states is large during 1 cycle.

Keywords Oscillatory shear stress · Stress decomposition · Brownian dynamics simulation · Double peaks

Introduction

Small amplitude oscillatory shear (SAOS) flow is widely used due to its simplicity and its ease of analysis. Fundamental rheological properties such as storage modulus (G') and loss modulus (G") are obtained through SAOS analysis, allowing the extent of elastic or viscous characteristics in various material systems to be evaluated. However, when strain amplitude (γ_0) is large, shear stress is no longer linear and has high harmonic contributions. Though it is not easy to deal with nonlinear behaviors, it is useful and informative to know the response of a material in the large amplitude oscillatory shear (LAOS) regime (Hyun et al. 2011).

To analyze nonlinear stress, several methods have been suggested by using Fourier transform (FT), characteristic functions, and Q parameter, and etc. (Wilhelm 2002; Klein et al. 2007; Hyun and Wilhelm 2009). One method to examine oscillatory shear stress is the stress decomposition method (Cho et al. 2005). It divides the total shear stress into elastic stress and viscous stress. If strain and strain rate are defined as $x = \gamma = \gamma_0 \sin \omega t$ and $y = \dot{\gamma}/\omega = \gamma_0 \cos \omega t$, respectively, then

$$\sigma(x,y) = \frac{\sigma(x,y) + \sigma(x,-y)}{2} + \frac{\sigma(x,y) + \sigma(-x,y)}{2} = \sigma_e(x,y) + \sigma_v(x,y) \quad (1)$$

where σ_e indicates the elastic stress and σ_v the viscous stress. This method can be expanded by using the Chebyshev polynomial (Ewoldt et al. 2008).

$$\sigma_e(x) = \gamma_0 \sum_{n=\text{odd}} e_n(\omega,\gamma_0) T_n(x) \quad (2)$$

$$\sigma_v(y) = \dot{\gamma}_0 \sum_{n=\text{odd}} v_n(\omega,\gamma_0) T_n(y) \quad (3)$$

Here, $e_n(\omega,\gamma_0)$, $v_n(\omega,\gamma_0)$, and T_n refer elastic Chebyshev coefficients, viscous Chebyshev coefficients, and nth order Chebyshev polynomial, respectively. By analyzing elastic and viscous stress or Chebyshev coefficients, the characteristic of nonlinear stress in various systems have been investigated (Salehiyan et al. 2015; Lee et al. 2015; Park et al. 2015; Khandavalli et al. 2016; Huang et al. 2017; Goudoulas and Germann 2017). Nam et al. (2011) applied the stress decomposition method to hard sphere systems; poly(methyl

✉ Kyung Hyun Ahn
ahnnet@snu.ac.kr

[1] School of Chemical and Biological Engineering, Institute of Chemical Processes, Seoul National University, Seoul 151-744, Republic of Korea

methacrylate) (PMMA) particles with average diameter of 10 μm dispersed in polybutene (PB) with molecular weight 920 g/mol at volume fraction 0.514. They observed double peaks in elastic stress near the flow reversal (FR) point. However, that observation has not been reported further, and its structural origin has never been explored.

Particulate fluids are receiving wide attention due to many practical applications (Lee et al. 2017). The behaviors of hard sphere systems under oscillatory shear flow have also been studied extensively, both experimentally and via simulation (Petekidis et al. 2003; McMullan and Wagner 2009; Besseling et al. 2012; Koumakis et al. 2013; Koumakis et al. 2016). However, most studies concentrate on a system with the volume fraction near the freezing point where interesting rheological behaviors such as yielding or ordering are observed under oscillatory shear flow, and there exists only a few studies at intermediate volume fractions.

In soft particle systems, there are many reports, especially experimental studies, in which soft particle systems are analyzed by adopting a hard sphere model (Mason et al. 1997; Senff and Richtering 1999; Fuchs and Ballauff 2005; Siebenburger et al. 2009; Mohan et al. 2013; Pellet and Cloitre 2016). In simulations, soft sphere systems tends to be described by using inverse-power potential (IPP), which controls the slope of the potential (Heyes and Brańka 2005, 2008; Pieprzyk et al. 2014).

Comparisons of soft and hard sphere systems are also reported; however, they concentrate on yielding behavior at high volume fractions (Grand and Petekidis 2008; Koumakis et al. 2012; Poulos et al. 2015) or concentrate on the rheological properties under simple shear flow (Nazockdast and Morris 2012; Ding and Mittal 2015). Thus, characteristics at an intermediate volume fraction, which is lower than the freezing point, need to be investigated further under the oscillatory shear flow. Though the structure of hard sphere systems under oscillatory shear flow at an intermediate volume fraction has been described (Lin et al. 2013; Wang and Swan 2016), analyzing oscillatory shear stress through stress decomposition at intermediate volume fraction needs to be studied further.

In this paper, the stress responses of both hard and soft sphere systems at an intermediate volume fraction under oscillatory shear flow are analyzed by using the particle simulation technique. We will inceptively inspect whether double peaks, which are observed in experiments of hard sphere systems, are also created in simulation. In addition, the obtained double peaks will be quantified and their structural origin will be explored.

This paper is composed as follows. First, oscillatory shear stress for both hard and soft spheres will be analyzed by performing stress decomposition. Next, it will be shown that double peaks appear only for hard sphere systems, and they will be quantitatively analyzed. Then, the stress and structure of both hard and soft sphere systems will be compared at the same normalized volume fraction, frequency, and γ_0. Finally, the stress and structure of hard spheres at different γ_0 are compared at the same volume fraction and frequency. We draw conclusions based on the results of the comparative study.

Simulation system

There are many simulation methods for colloidal dispersions such as Brownian dynamics (BD), Stokesian dynamics (SD), multi-particle collision dynamics (MPCD), etc. (Foss and Brady 2000a, b; Gompper et al. 2009; Park et al. 2016). In this study, due to plenty of reliable references, applicability to various systems, and relatively low computational cost, a BD simulation technique is used. Hydrodynamic, potential, and Brownian forces affect the motion of the particles. The governing equation is the Langevin equation, as given in Eq. 4.

$$m\frac{\mathrm{d}\mathbf{v}_i}{\mathrm{dt}} = \mathbf{F}_i^H + \mathbf{F}_i^P + \mathbf{F}_i^B \tag{4}$$

where, m, $\boldsymbol{v}_i$, $\boldsymbol{F}_i^H$, $\boldsymbol{F}_i^P$, and $\boldsymbol{F}_i^B$ are the mass of a particle, velocity vector, hydrodynamic force, potential force, and Brownian force of the ith particle, respectively. The left-hand side term can be neglected when the time scale is sufficiently long to relax particle momentum. When the particle is a sphere, hydrodynamic force is expressed as given in Eq. 5.

$$\mathbf{F}_i^H = -6\pi\eta a\left(\mathbf{v}_i - \mathbf{v}_i^\infty\right) \tag{5}$$

where, η, a, and $\mathbf{v}_i^\infty$ are the medium viscosity, radius of particle, and imposed flow velocity at ith particle, respectively. In this simulation, oscillatory shear flow $\mathbf{v}_i^\infty = \dot{\Gamma}_0 \cdot \mathbf{x}\, cos\omega t$ is imposed, where $\dot{\Gamma}_0$, $\mathbf{x}$, and ω are the velocity gradient tensor, the position of particle and frequency, respectively.

Brownian is defined by Eqs. 6 and 7.

$$\left\langle \mathbf{F}_i^B(t) \right\rangle = 0 \tag{6}$$

$$\left\langle \mathbf{F}_i^B(t)\mathbf{F}_i^B\left(t'\right) \right\rangle = 12k_BT\pi\eta a\delta\left(t - t'\right)\mathbf{I} \tag{7}$$

where, bracket indicates an ensemble average. Here, k_B, T, $\delta(t)$, and $\mathbf{I}$ are the Boltzmann constant, temperature, Dirac delta function and unit tensor, respectively. It can be expressed by Wiener process as in Eq. 8.

$$\mathbf{F}_i^B(t)\Delta t = \sqrt{2k_BT\zeta}\Delta\mathbf{W}_i(t) \tag{8}$$

where, $\langle \Delta\mathbf{W}_i(t) \rangle = 0$ and $\langle \Delta\mathbf{W}_i(t)\Delta\mathbf{W}_i(t') \rangle = \delta(\mathrm{t} - \mathrm{t}')\mathbf{I}\Delta\mathrm{t}$ are satisfied.

Langevin equation can be rearranged as Eq. 9 by using previous equations, and particle position is updated by using this equation at each time step (Δt).

$$\Delta \mathbf{x}_i = \left[\mathbf{v}^{\infty}(\mathbf{x}_i) + \frac{1}{6\pi\eta a}\mathbf{F}_i^{p}\right]\Delta t + \sqrt{2k_BT/6\pi\eta a}\,\Delta \mathbf{W}_t \quad (9)$$

One method used to describe hard sphere system is the potential-free (PF) method (Heyes and Melrose 1993; Foss and Brady 2000a; Wang and Swan 2016). In this method, the particles are moved by the force from the imposed flow and Brownian motion, and overlapped particles are relocated to non-overlapped states. The moving distance of the overlapped particle is determined by Eq. 10.

$$\Delta x^{\mathrm{HS}} = k\hat{\mathbf{r}}(\Delta r - 2a)H(2a - \Delta r) \quad (10)$$

where, Δx^{HS}, Δr, H, and k indicate hard sphere displacement, the center-to-center distance between overlapped particles, Heaviside step function, and a constant that defines how far the overlapped particles are moved to the non-overlapped state, respectively. Moreover, $\hat{\mathbf{r}}$ denotes a unit vector $\boldsymbol{r}/r$. To prevent overlap, k should be larger than 0.5. When it is 0.5, the overlapped particles are relocated to contact distance, and when k is 1, the overlapped particle are relocated to a non-overlapped state as much as their overlapped distance. In this simulation, k is set as 1 (Heyes and Melrose 1993). Interparticle force in PF is given as Eq. 11.

$$\mathbf{F}_i^{P} = 6\pi\eta a\frac{\Delta x^{HS}}{\Delta t} \quad (11)$$

In PF, the particle stress from the interparticle force is calculated by using the radial distribution function (RDF) at contact distance ($2a$) as in Eq. 12 (Foss and Brady 2000a).

$$\left\langle \boldsymbol{\Sigma}_p \right\rangle = -n^2 k_B T a \int_{r=2a} \hat{\mathbf{r}}\hat{\mathbf{r}} g(\mathbf{r}) dS \quad (12)$$

where g($\mathbf{r}$) and n indicate RDF and the number of particles, respectively. To change particle softness, the IPP method is used, as presented in Eq. 13 (Mitchell et al. 1995).

$$\varepsilon(r) = k_BT\left(\frac{2a}{r}\right)^{n} \quad (13)$$

When the slope n is smaller than or equal to 12, it shows soft sphere characteristics. On the contrary, when n is larger than or equal to 18, it shows hard sphere characteristics (Brańka and Heyes 2006; Lange et al. 2009). When n is larger than 72, transport coefficients are hardly distinguishable at different n, and this potential describes true hard sphere systems as n goes to infinity. (Heyes and Brańka 2005). In this paper, n is 8 for soft spheres and 54 for hard spheres. Interparticle in IPP is given in Eq. 14.

$$\mathbf{F}_i^{P} = -\sum_{i\neq j}\frac{d}{d\mathbf{x}}\varepsilon\left(\left|\mathbf{x}_i - \mathbf{x}_j\right|\right) \quad (14)$$

Stress is obtained from the distance between two particles and the interparticle force in IPP as in eq. 15.

$$\left\langle \boldsymbol{\Sigma}_p \right\rangle = -n\left\langle \mathbf{x}\mathbf{F}^{P} \right\rangle \quad (15)$$

To describe hard spheres, an IPP with a slope of 54 and PF are used, whereas an IPP with a slope of 8 is used to describe soft spheres.

To revise the volume fraction of systems with different particle softness, a reduced coupling parameter ($\Gamma/\Gamma_{\mathrm{freezing}}$) is used. The effective volume fraction (Γ) is normalized by the volume fraction at the freezing point ($\Gamma_{\mathrm{freezing}}$) of each system. It is reported that reduced transport coefficients at equilibrium or in simple shear can be plotted on a master curve when plotting as a function of the reduced coupling parameter (Lange et al. 2009; Ding and Mittal 2015). As this value indicates how far the system is away from the freezing point, it is a useful parameter when comparing systems with different particle softness. The freezing point at specific slope n can be found in the previous paper (Agrawal and Kofke 1995). For example, the freezing point corresponds to volume fractions 0.494, 0.493, and 0.827 for the PF, IPP with $n = 54$, and IPP with $n = 8$, respectively.

Pair distribution function (g($\mathbf{r}$)) can be expressed as a series of spherical harmonic function series as in Eq. 16 (Hanley et al. 1987), and $g_{2,-2}(r)$, which is closely related with shear stress, can be calculated at each time for investigating the microstructure.

$$g(\mathbf{r}) = g_s(r) + \sum_{l=1}^{\infty}\sum_{m=-l}^{l} g_{lm}(r)Y_{lm}(\theta,\varphi) \quad (16)$$

Moreover, to quantify the extent of particle ordering, the concept of two-body excess entropy is adopted (Truskett et al. 2000; Ding and Mittal 2015). Two-body excess entropy represents full excess entropy of the whole system (Dzugutov 1996). It can be obtained by using RDF and particle number density. This approach has advantages because the structure under oscillatory shear flow, whose structure varies as time proceeds, can be quantified as a single value at a given time as in Eq. 17.

$$s_2 = -\frac{\rho}{2}\int\{g(\mathbf{r})\ln g(\mathbf{r}) - [g(\mathbf{r}) - 1]\}d\mathbf{r} \quad (17)$$

where g($\mathbf{r}$) is RDF and ρ is number density. When $-s_2$ goes to infinity, it implies a highly ordered structure. When it is near zero, it implies a totally disordered structure. The extent of particle alignment during the cycle is evaluated by using this value.

In this paper, the number of particles is 25^3. All particles are allocated in the lattice and the initial configuration is obtained after an equilibration step. Subsequently, simulations are conducted at every γ_0 and frequency (ω) from this initial configuration. The Lees-Edwards periodic boundary condition is used when shearing (Lees and Edwards 1972). ω is normalized by multiplying it by the particle characteristic time ($6\pi a^3\eta/k_BT$). Normalized ω can be defined as the Deborah number.

$$\mathrm{De} = 6\pi a^3\omega\eta/k_BT \tag{18}$$

In this simulation, $\Gamma/\Gamma_{\mathrm{freezing}}$ is fixed at 0.61 (Γ of hard sphere: 0.3, soft sphere: 0.5), and the range of De is from 20 to 100 (mostly De = 80). The stress in each oscillatory shear test is obtained by averaging the stresses during the 7 cycles after the stress is stabilized.

Stress decomposition and double peaks

Total, elastic, and viscous stresses

Figure 1a shows the total, elastic, and viscous stresses in a wide range of γ_0 at $\Gamma/\Gamma_{\mathrm{freezing}} = 0.61$ and De = 80 from the PF that corresponds to a hard sphere system. Figure 1b shows the elastic stresses for De from 20 to 100. Here, all stresses are normalized by their maxima.

As γ_0 increases, the total stress becomes distorted, followed by a shape change in the elastic and viscous stresses. As shown in previous studies (Koumakis et al. 2012; Koumakis et al. 2013), total stress overshoot is not observed. It is to be noted that double peaks are observed in the elastic stress near flow reversal when γ_0 is large, and this has rarely been reported. The double peaks are also observed in experimental with hard spheres (Nam et al. 2011). As seen in Fig. 1b, the double peaks appear over a wide range of De values at intermediate γ_0 in this simulation.

By increasing the slope of IPP, the particles change from soft to hard spheres. The total, elastic, and viscous stresses are shown in Fig. 2. In this simulation, the particles are soft when the slope of IPP is 8, and hard when the slope of IPP is 54. The $\Gamma/\Gamma_{\mathrm{freezing}}$ is fixed to 0.61 as in the PF case. It is to be noted that the actual volume fractions are different in hard and soft sphere systems.

As γ_0 increases, the shape of the total, elastic, and viscous stresses changes in both cases. At high γ_0, the shape of total stress is governed by that of viscous stress. However, in Mohan et al. (2013) and Koumakis et al. (2013), most of the stress comes from the elastic contribution. This difference can be explained by the difference in volume fraction (Poulos et al. 2015). At high volume fraction, elastic characteristic is dominant (Mohan et al. 2013), while viscous characteristic is dominant (this paper) at intermediate volume fraction. For soft spheres, double peaks are not observed in elastic stress (Fig. 2a). In contrast, in Fig. 2b, which describes a quasi-hard sphere system, double peaks are observed in elastic stress and the shape of each stress is similar to that presented in Fig. 1a which uses PF. From these results, it can be inferred that double peaks appear only in simulations that describe hard sphere system.

Peaks characteristics

To quantify the characteristics of the double peaks, both depth and width are defined as shown in Fig. 3, in which the elastic stress is plotted at $\Gamma/\Gamma_{\mathrm{freezing}} = 0.61$, De = 80, and $\gamma_0 = 3$. The horizontal axis is time, which is normalized by the duration of 1 cycle. The vertical axis is the elastic stress, which is normalized by its maximum. The depth is defined as the gap between the normalized elastic stress at peak and that at the local minimum (at normalized time of 0.25). The width is the normalized time interval between the two peaks.

In this simulation, double peaks are observed only in the hard sphere system (i.e., PF or IPP; $n = 54$). The γ_0 range in which double peaks appear is wider when using PF, which better describes a hard sphere, than for the case of IPP with a slope of 54 (not shown in this paper). In Fig. 4, the open symbols connected with black solid lines represent the results

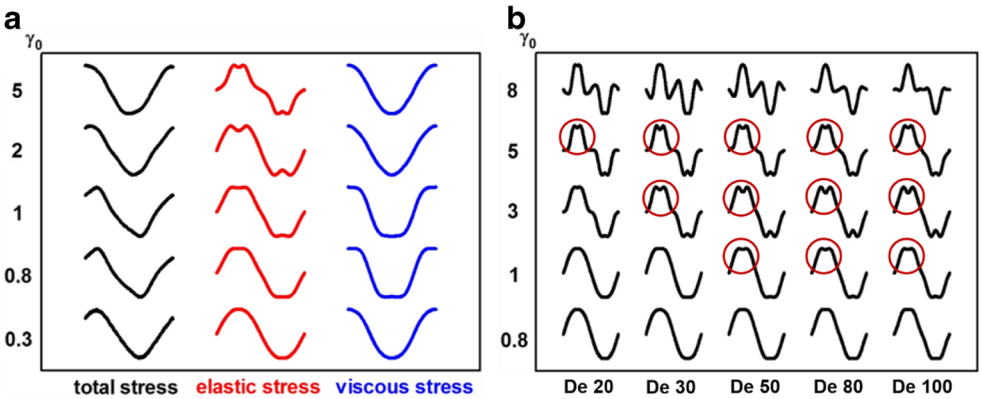

Fig. 1 **a** The total, elastic, and viscous stresses at De = 80; **b** elastic stresses from De = 20 to 100 for PF at $\Gamma/\Gamma_{\mathrm{freezing}} = 0.61$.

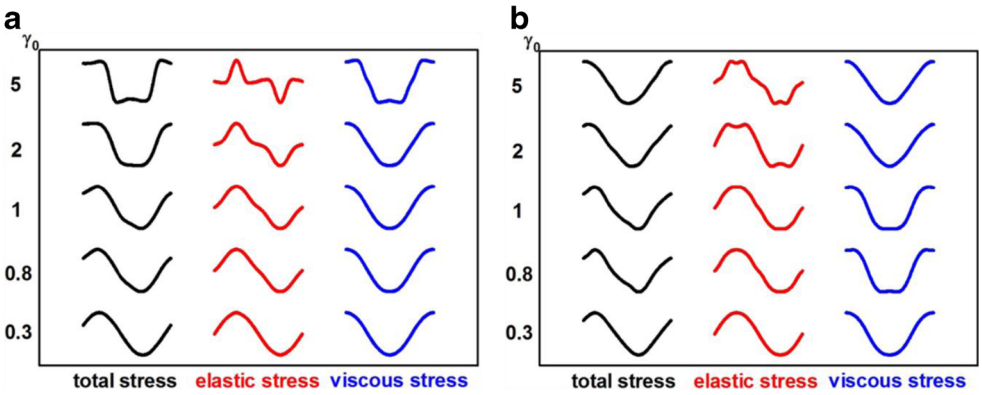

Fig. 2 The total, elastic, and viscous stresses for **a** $n = 8$ (soft sphere), **b** $n = 54$ (quasi-hard sphere) for IPP method, at $\Gamma/\Gamma_{freezing} = 0.61$ and De = 80

from PF, while the filled symbols connected by red dashed lines represent the results from IPP.

Both depth and width show maxima, and there is a range of γ_0, beyond which the peaks disappear. The depth from PF, which has better hard sphere characteristics, is larger than that obtained from IPP. The maximum locates at $\gamma_0 = 3$. For width, the variation is less pronounced, and the maximum is observed at $\gamma_0 = 2$.

Stress and structure analysis

Soft and hard spheres

The stress and structure of a hard sphere system, which shows double peaks, and a soft sphere system, which does not show double peaks, are compared when $\Gamma/\Gamma_{freezing}$, De, and γ_0 are 0.61, 80, and 3, respectively. In this case, the hard sphere system is simulated using PF, and soft sphere system using IPP with $n = 8$. In Fig. 5a, the solid curves indicate total stress, and the dashed curves indicate elastic stress. The black curve is for the soft sphere system (IPP; $n = 8$) and the red one is for the hard sphere system (PF). The total and elastic stresses are normalized by the maximum value of the total stress for each system. The blue columns indicate the regime between two peaks. Point A represents the first peak before FR, and point B

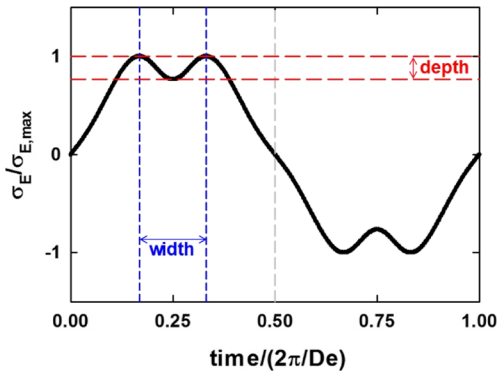

Fig. 3 The definition of depth and width when double peaks appear

represents the second peak after FR. In Fig. 5b, $g_{2,-2}$ at points A, flow reversal (FR), and B are shown. Solid line indicates hard sphere and dashed line indicates soft sphere. As the effective radius r in RDF can vary with particle softness, it is necessary to amend the radius. In this study, r is revised according to $\Gamma_{\mathrm{rel}}^{1/3} = \left(\Gamma/\Gamma^{\mathrm{HS},freezing}\right)^{1/3}$ (Lange et al. 2009). Here, $\Gamma^{\mathrm{HS,\ freezing}}$ indicates the volume fraction at the freezing point of the hard sphere system.

In Fig. 5a, shape differences between the total stress of soft and hard spheres may be clearly observed in the regime where double peaks appear. The shape differences are not significant in the rest of the time domain. The differences in total stress in the blue regime also affect the elastic stress. Bases on the shape of the stress, double peaks appear when the total stress decreases rapidly before FR, which is followed by a gradual decrease after FR. In Fig. 5b, the first peak shows a negative value before flow reversal point (point A) and flow reversal point (FR), whereas it shows a positive value after flow reversal (point B). These results imply that the particle structure along the compressional axis before flow reversal is still maintained at flow reversal, whereas it is oppositely relocated along the compressional axis after flow reversal. $g_{2,-2}$, which is closely related with the shear stress, shows a large difference between soft and hard sphere systems. For hard spheres, a sharp peak is shown near the contact point (2a, $r\Gamma_{rel}^{1/3} \approx 1.69$) whereas the position of $g_{2,-2}$ peak varies and the peak is broad for soft spheres. To obtain more information on the origin of two peaks, the structures of the hard and soft spheres at points A and B, which represent the two peak points, are compared.

Initially, the pair distribution function (PDF) needs to be inspected. The particles within a distance $\pm 5a$ on the velocity-velocity gradient plane ($-5a < x, y < 5a$) and $\pm 0.05a$ ($-0.05a < z < 0.05a$) to the vorticity direction relative to the reference particle are analyzed. Note that two systems have the same $\Gamma/\Gamma_{freezing}$. Figure 6a, c, e shows the results for soft spheres, while Fig. 6b, d, f show the results for hard spheres. Figure 6a, b shows the results obtained at point A in Fig. 5, while Fig. 6e, f are the results obtained at point B. Figure 6c, d

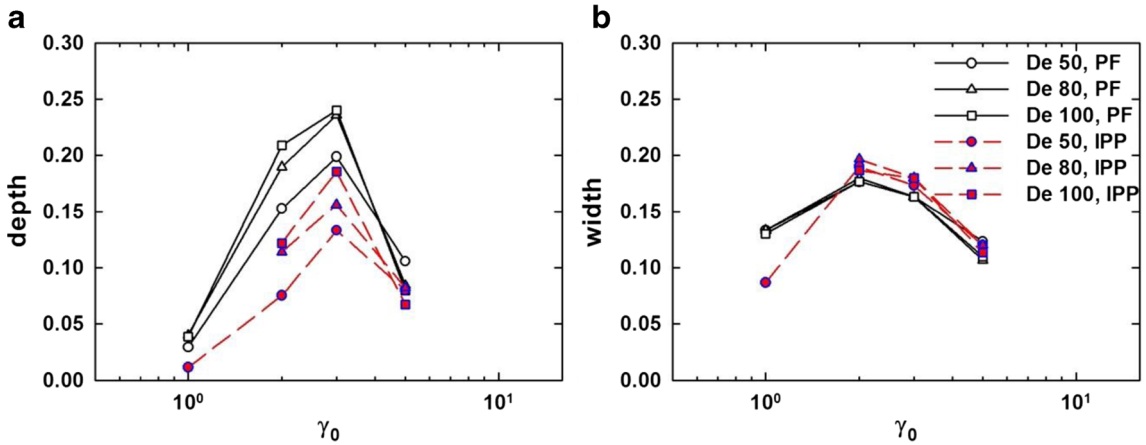

Fig. 4 Double peaks **a** depth and **b** width at De = 50, 80, and 100 as a function of γ_0 for PF and IPP with $n = 54$

shows the results obtained at flow reversal point. In Fig. 6, the more reddish the PDF is, the more possibility that there is a particle at that point. Likewise, the more bluish the PDF is, the less possibility that there is a particle at that point. The circle at the center indicates double of the particle size. At point A in Fig. 5, the flow direction is from left to right, and at point B, the flow direction is from right to left.

In both cases, the particles are aligned to the compressional axis and are scarcely aligned along the extensional axis. As shown in Fig. 5b, the particle structure along the compressional axis is maintained at flow reversal point for both soft and hard sphere systems, whereas the structure along the opposite direction is observed at point B. A lot of particles are in touch for hard spheres (as evidenced by red color at contact), while particle density at contact is small (a red point is not observed at contact) and alignment to the flow direction is insignificant for soft spheres. Though not included in this paper, the difference in alignment is observed not only at points A, B, and flow reversal points but also during the whole cycle. As time proceeds from point A to point B, the particles are found less at contact distance for the hard sphere system (number of red point decreases), while for the soft sphere, the value of r of overlapped particles increases (points in inner circle area decreases), which leads the particles to locate more near the circle (contact distance). Next, the radial distribution function (RDF) at the two points is inspected. The RDF is plotted in Fig. 7. Here, only the first half cycle ($0 < \text{time}/(2\pi/\text{De}) < 0.5$) is plotted. To help comprehension, points A, B, and FR are also indicated. Legends indicate the value of g(**r**).

For hard spheres, the particles do not exist in the inner area, $r\Gamma_{rel}^{1/3}$ is less than 1.69, which is the contact point. For soft spheres, the particles are observed in the inner area and the minimum $r\Gamma_{rel}^{1/3}$ of particle observation is changed with time. The maximum g(**r**) at each time is much higher throughout the cycle in hard sphere systems. Maximum g(**r**) is observed at contact point (2a, $r\Gamma_{rel}^{1/3} \approx 1.69$) for hard spheres, while g(**r**) increases with $r\Gamma_{rel}^{1/3}$ and maximum g(**r**) does not coincide with the contact distance for soft spheres. These results correspond to Fig. 5b as well as previous numerical studies, which show structures of soft and hard sphere systems in simple shear (Nazockdast and Morris 2012; Ding and Mittal 2015).

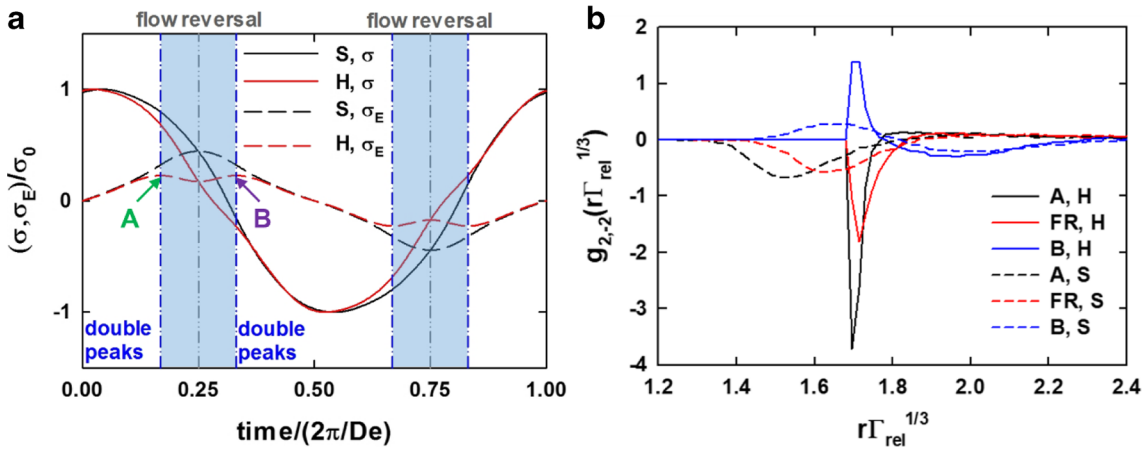

Fig. 5 **a** The total and elastic stresses of soft sphere (S, IPP; $n = 8$) and hard sphere (H, PF) systems, **b** $g_{2,-2}$ at points A, flow reversal (FR), and B for soft sphere and hard sphere systems when $\Gamma/\Gamma_{freezing} = 0.61$, De = 80, and $\gamma_0 = 3$.

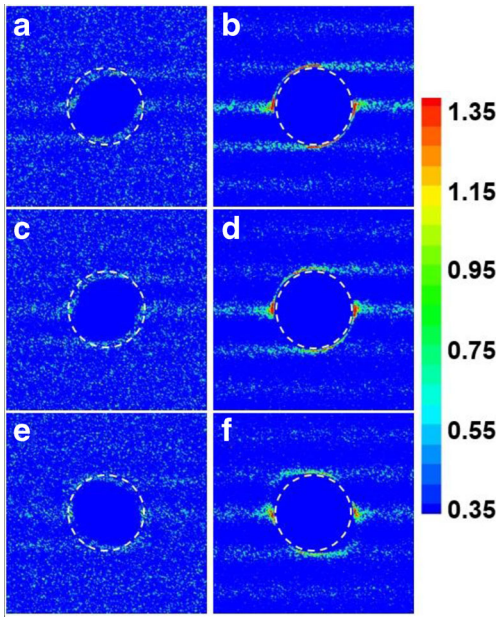

Fig. 6 PDF of **a** point A of soft sphere, **b** point A of hard sphere, **c** flow reversal point of soft sphere, **d** flow reversal point of hard sphere, **e** point B of soft sphere, and **f** point B of hard sphere

In the soft sphere system, maximum g(**r**) throughout the cycle is observed after flow reversal. On the contrary, in the hard sphere systems, minimum g(**r**) at contact throughout the cycle is observed after flow reversal. As can be verified in Fig. 7, the structure formation and deformation of the particles during the whole cycle are different between two systems.

As the first peak of RDF is important for the particle system, the values of r and g(**r**) at the first peak during the cycle are also tracked in Fig. 8. The black symbols are for the soft sphere system, while the red symbols for the hard sphere system. The open symbols represent the results before FR, while the filled symbols are the results after FR. Only the results during a half cycle are plotted because the results after FR are the same as before FR. The solid arrows are guidelines that show the path before FR, while the dashed arrows are the guidelines that show the path after FR.

For soft spheres, the variation of r is more pronounced than that of g(**r**) at the first peak. In contrast, for hard spheres, the variation of g(**r**) is more pronounced than that of r. When compressive force is imposed to hard spheres, most particles are located in near contact ($2a$, $r\dot{\Gamma}_{rel}^{1/3} \approx 1.69$). In contrast, soft spheres can overlap, which may causes particle distribution around $r\dot{\Gamma}_{rel}^{1/3}$. Note that the direction of force from the flow field and the interparticle force is opposite to the compressional axis. When the flow is weakened, compressed particles are pushed away as the interparticle force becomes comparatively stronger.

For soft spheres, which are indicated by the black symbols in Fig. 8, at the initial stage of the cycle where the flow is strong, the g(**r**) does not change much and the particles are compressed to each other. At the latter stage before FR, as the flow is weakened, the closely located particles are moved away from each other. Therefore, g(**r**) increases only slightly and r increases a lot. These processes are represented by arrows 1 and 2 in Fig. 8, which indicates the change of RDF before FR, which is in accordance with Fig. 7a. Shortly after FR, though flow direction is reversed, the structure formed in the previous compressional axis is maintained. As time proceeds, this maintained structure is pushed away to the extensional axis of reversed flow field (previous compressional axis), which makes both g(**r**) and r increase. Then the particles are spread out and no significant structure is formed. Thus, g(**r**) increases followed by a decrease while r increases. Long after FR, as the particles are affected continuously by the flow, the particles begin to compress again and, as a result, r continuously decreases. These processes correspond the arrows 3, 4, and 5 in the figure, which indicate the change of RDF after FR.

For a hard sphere system, which is indicated by red symbols in Fig. 8, the value of g(**r**) at contact is quite large at the initial stage of the cycle. As time proceeds and approaches FR, the flow velocity is reduced, which reduces compressive forces so that the particles are pushed away from each other, in a manner similar to relaxation in an equilibrium state. Therefore, r increases slightly and g(**r**) decreases significantly. These processes are represented by the arrows 1 and 2 in Fig. 8, which indicates the change of RDF before FR, which is in accordance with Fig. 7b. As the flow changes direction after

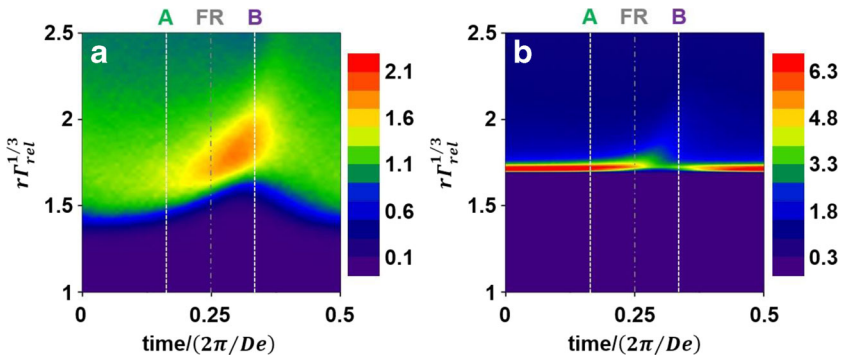

Fig. 7 RDF of **a** soft sphere and **b** hard sphere as time proceeds. The white dashed lines represent points A and B (peaks point), and the dark gray dash-dot line represents flow reversal (FR) point. Note that the legend of soft and hard sphere systems are different

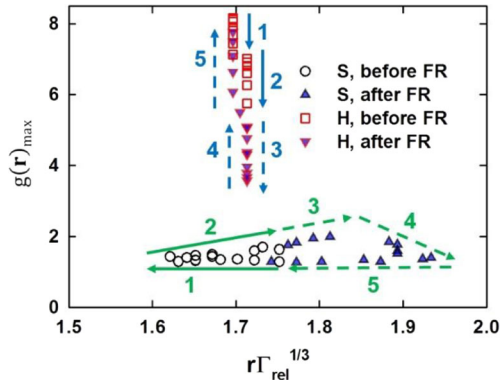

Fig. 8 The location of the first peak in RDF during a half cycle in both soft (S, IPP; $n = 8$) and hard sphere (H, PF) systems

FR, the particles, which are aligned to the compressional axis before FR, become realigned in the opposite direction for a while, and shortly after FR, the value of g(**r**) near the contact point decreases continuously. As the flow becomes stronger away from FR, the particles are compressed again at the contact point. Therefore, the value of r is the same as that at contact location and g(**r**) increases. These processes correspond the arrows 3, 4, and 5 in the figure, which indicate the change of RDF after FR.

Due to the differences in overall structural alignment of the particles as seen in PDF and the differences in structure formation and deformation mechanism during the cycle as can be seen in RDF, soft sphere systems do not show double peaks, but they appear in hard sphere system.

Hard sphere at different strain amplitudes

In this section, the stress and structure of the hard sphere system at two γ_0, one with double peaks and the other without, are compared. The simulation is performed with PF at $\Gamma/\Gamma_{freezing} = 0.61$ and De = 80. In this condition, double peaks are observed in the range of γ_0 from 1 to 5. To compare cases in which double peaks appear and not, $\gamma_0 = 0.8$ and $\gamma_0 = 1$ are selected as low γ_0. Likewise, $\gamma_0 = 5$ and $\gamma_0 = 8$, are selected as high γ_0. The stresses at those four γ_0 are compared by pairing two by two. Fig. 9a shows the total and elastic stress at $\gamma_0 =$ 0.8 and 1, and points C and D indicate the first and second peak, respectively, at $\gamma_0 = 1$. Fig. 9b shows the total and elastic stress at $\gamma_0 = 5$ and 8, and points E and F indicate the first and the second peak, respectively, at $\gamma_0 = 5$. The black curves indicate a condition in which double peaks do not appear, while the red curves indicate a condition in which double peaks

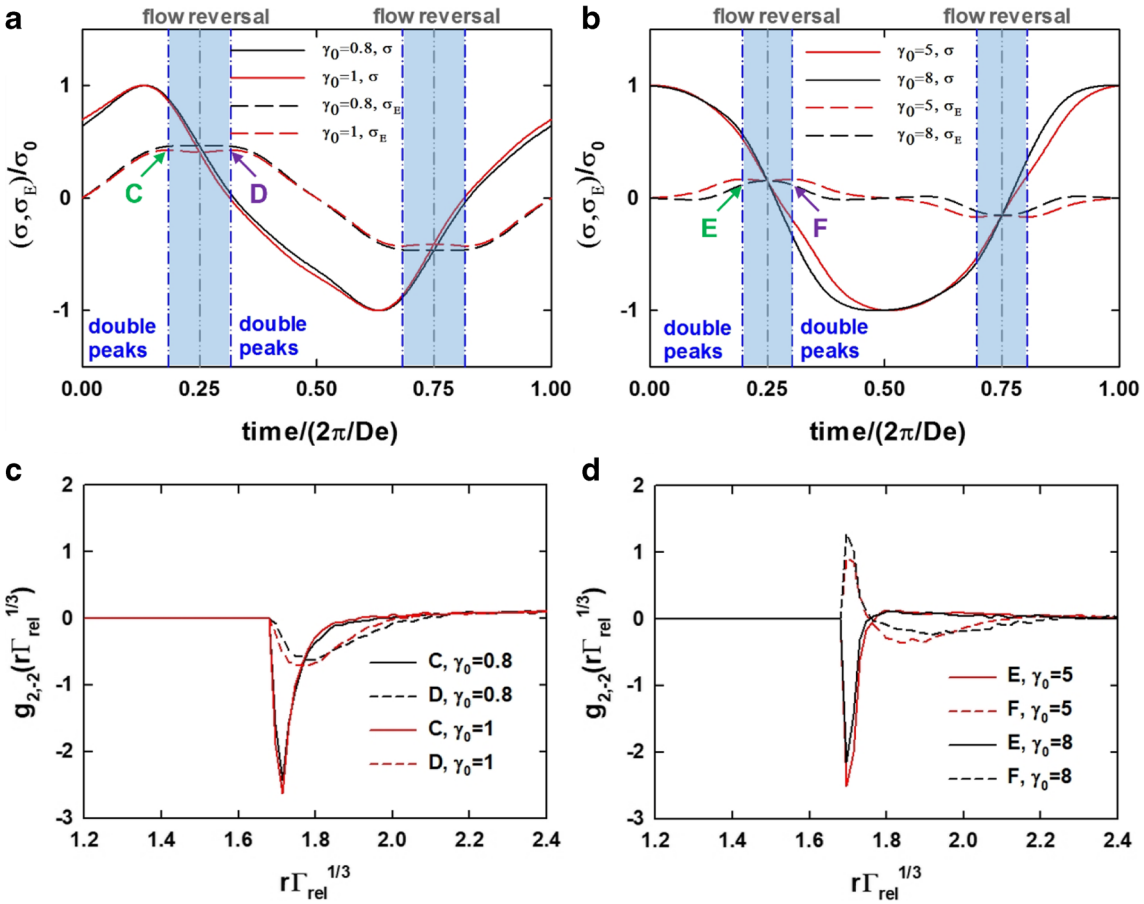

Fig. 9 **a** Total and elastic stresses at $\gamma_0 = 0.8$ and 1, **b** total and elastic stresses at $\gamma_0 = 5$ and 8, **c** $g_{2,-2}$ for points C and D at $\gamma_0 = 0.8$ and 1, and **d** $g_{2,-2}$ for points E and F at $\gamma_0 = 5$ and 8. Double peaks are not observed at $\gamma_0 = 0.8$ and 8, but double peaks are observed at $\gamma_0 = 1$ and 5.

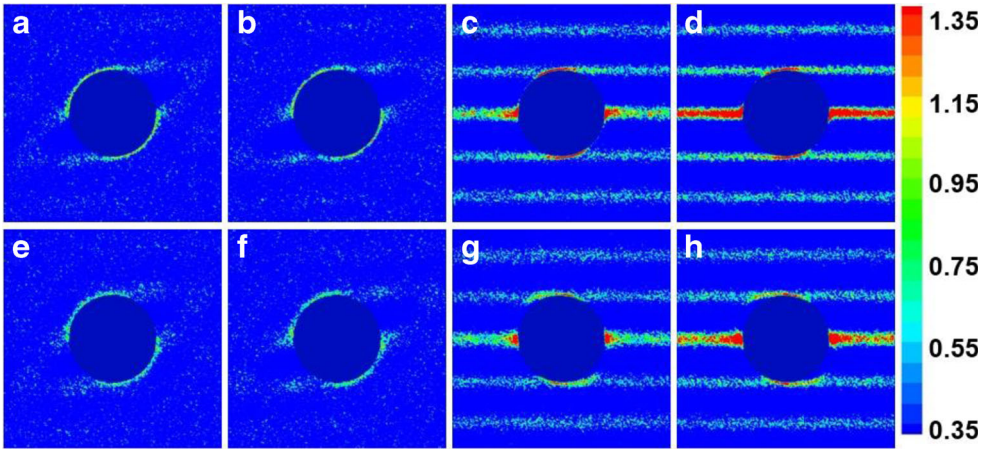

Fig. 10 PDF for (a) $\gamma_0 = 0.8$, point C, (b) $\gamma_0 = 1$, point C, (c) $\gamma_0 = 5$, point E, (d) $\gamma_0 = 8$, point E, (e) $\gamma_0 = 0.8$, point D, (f) $\gamma_0 = 1$, point D, (g) $\gamma_0 = 5$, point F, (h) $\gamma_0 = 8$, point F

appear. The solid lines represent total stress, and the dashed lines represent elastic stress. All stresses are normalized by the maximum of the total stress at each γ_0. Fig. 9c shows $g_{2,-2}$ for points C and D at $\gamma_0 = 0.8$ and 1. Fig. 9d shows $g_{2,-2}$ for points E and F at $\gamma_0 = 5$ and 8. The solid lines represent before flow reversal, and the dashed lines represent after flow reversal regime.

The total stress shows little differences in the regimes represented by the blue columns. $g_{2,-2}$ at two paired γ_0 are similar as total stresses is similar for the two γ_0 (especially at points C and E, which are the peak points before flow reversal). For $g_{2,-2}$ at points D and F, which are the peak points after flow reversal, the first peak of point D is negative, whereas that of point F is positive. It means that the particle structure along the compressional axis before flow reversal is maintained at point C due to small strain rate even though the flow direction is reversed, whereas the structure is realigned to the compressional axis after flow reversal due to large strain rate at point D. The PDF obtained at peak points are illustrated in Fig. 10.

As γ_0 increases, more particles are aligned to the compressional axis or flow direction. As confirmed in Fig. 9c and d, the structure at point D shows the same directional alignment to that of point C, whereas the structure at point F shows the opposite directional alignment to that of point E. The structures, whether double peaks appear ($\gamma_0 = 1$ or 5) or not ($\gamma_0 = 0.8$ or 8), are not much different. It is notable that the PDF at points C and D and that at points E and F are clearly different, even though the elastic stresses are the same. Though not included in the paper, the average angles at contact distance ($2a$) are almost same at the same time for the two γ_0 cases whether the double peaks appear or not. Moreover, the average angles at the point of same elastic stress (C and D / E and F) under the same γ_0 are different (not included in this paper). Thus, it is hard to match elastic stress and structure one-to-one at each time. So it will be necessary to adopt a different structure analysis tool to correlate elastic stress and structure.

The concept of two-body excess entropy is adopted as a new structural analysis method. This approach is useful because the structure under oscillatory shear flow, which varies with time, can be quantified as a single value at any time (Eq. 17). When the pair distribution function of every location is one, it means a totally disordered system and the excess entropy is zero. In contrast, when the excess entropy goes to

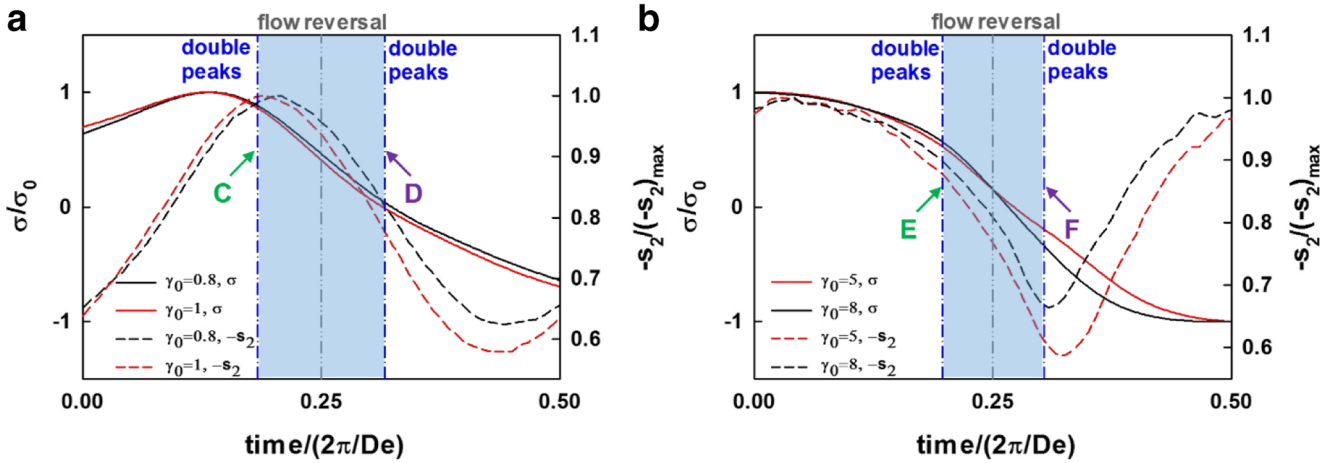

Fig. 11 Normalized total stress and excess entropy during half cycle at **a** $\gamma_0 = 0.8$ and 1 and **b** $\gamma_0 = 5$ and 8

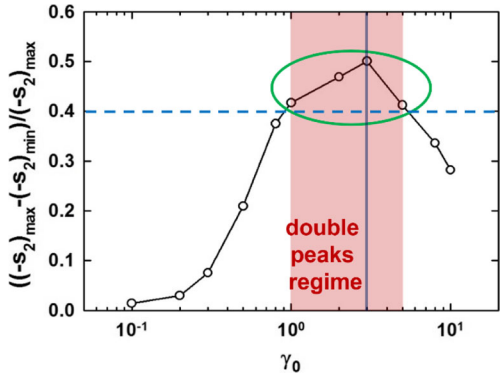

Fig. 12 The difference in the maximum and minimum of excess entropy as a function of γ_0.

minus infinity, it indicates a perfect crystal structure. Fig. 11a is the total stress and excess entropy for $\gamma_0 = 0.8$ and 1, while Fig. 11b presents those for $\gamma_0 = 5$ and 8. The solid lines represent the total stress, and the dashed lines represent the excess entropy. The red curves show the results with double peaks and the black curves show the results without double peaks. The total stress and excess entropy are normalized by their maxima.

Excess entropy shows a maximum before FR and minimum after FR. The moment of minimum excess entropy is observed earlier as γ_0 increases. This indicates that the rate of realignment to the opposite direction after FR becomes large as γ_0 increases. Although the total stress or other structural analysis are not so much different between the two γ_0, the difference in excess entropy is notable in the double peaks regime. The differences between the maximum and minimum of excess entropy are larger when double peaks appear (Fig. 11, red curves) than in the absence of double peaks (Fig. 11, black curves).

At maximum excess entropy, the particles are well-packed along the compressional axis and the structure is highly ordered. In contrast, the structure is poorly ordered at minimum excess entropy. The difference between the maximum and minimum of the normalized excess entropy is plotted as a function of γ_0 in Fig. 12. When this value is large, there exists a significant structural difference between two.

The difference between maximum and minimum excess entropy increases with the increase in γ_0, and the maximum is observed at $\gamma_0 = 3$, after which it decreases. In this simulation, double peaks are observed in the range of γ_0 from 1 to 5, as indicated in the red column of Fig. 12. When the difference between maximum and minimum exceeds a critical value (~0.4), double peaks appear. Thus, double peaks are observed only when the structural difference between the maximum-ordered state and the minimum-ordered state is large during the cycle. The subtracted excess entropy shows a similar curve with depth (Fig. 4a), which is one of the characteristic values of double peaks. Depth increases as γ_0 increases, and the maximum depth is observed at $\gamma_0 = 3$, after which it decreases. These characteristics (i.e., maxima at γ_0 = 3 and curve shape) are observed in both the depth of the elastic stress curve and in the results of quantitative structural analysis (excess entropy). And the extent of the difference between the maximum- and minimum-aligned states is related to the depth of the double peaks.

From the excess entropy results, double peaks are created when the structural difference is large during the oscillation. The variation of g(**r**) at contact is significant for hard sphere systems, which can lead double peaks to appear. This result also supports the observation that double peaks are observed when the structural difference during the cycle is large. Therefore, it can be concluded that double peaks appear at the systems that the difference between maximum- (before FR) and minimum-ordered states (after FR) is significant during the cycle.

Conclusions

It has been reported that double peaks are observed in elastic stress in experiments for hard sphere suspensions. However, the structural origin of those double peaks has not been reported and no quantification of the double peaks has been conducted. In this paper, to quantify the

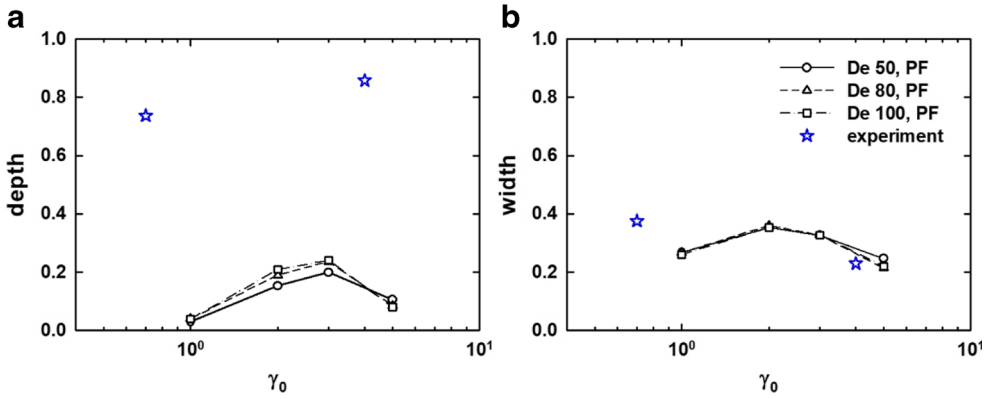

Fig. 13 Comparison of a) depth and b) width between simulation and experiment. Simulation data is obtained by using potential-free method (hard sphere), and experimental data is adopted from Nam et al. (2011)

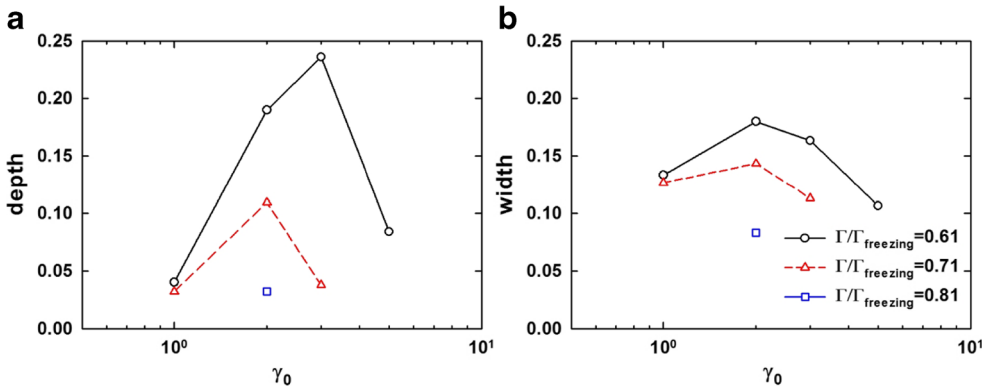

Fig. 14 Double peaks a) depth and b) width at De = 80 as a function of γ_0 for the potential-free method at $\Gamma/\Gamma_{freezing}$ = 0.61, 0.71 and 0.81

double peaks, their depth, and width are defined. The depth and widths of the double peaks were found to exhibit maxima with increased γ_0.

To investigate the structural origin of double peaks, PDF and the first peak of RDF for both soft and hard spheres were compared at the same $\Gamma/\Gamma_{freezing}$, ω, and γ_0. As a result, an overall structural difference during the cycle, a difference in structural formation before FR, and a deformation mechanism after FR were observed. These differences were found to determine the appearance of double peaks.

Structures of hard sphere systems at two γ_0, one that shows double peaks and the other does not, were compared at the same $\Gamma/\Gamma_{freezing}$ and ω. The structures at the same time but different γ_0 are not much different, but the structures at two peaks points at the same γ_0 are clearly different. Thus, it was hard to correlate the elastic stress and structure one-to-one at each time.

To correlate elastic stress with structure and to quantify the structure during a cycle, the concept of excess entropy was applied to the hard sphere system. By applying this concept, it was concluded that double peaks are observed when the structural difference between the maximum- and minimum-ordered states is large.

By inspecting the structure of hard and soft spheres and the structure of hard sphere system at different γ_0, the conditions for the presence of double peaks are suggested. Double peaks were observed when there is a large difference between the structure before FR, in which the particles are aligned to the compressional axis, and after FR, in which particle structure on previous compressional axis is broken.

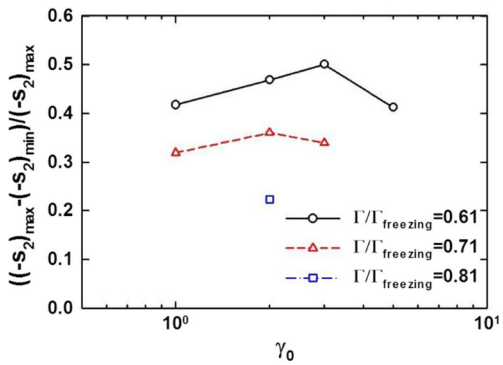

Fig. 15 The difference in the maximum and minimum of excess entropy as a function of γ_0 at $\Gamma/\Gamma_{freezing}$ = 0.61, 0.71 and 0.81

Funding information This work was supported by the National Research Foundation of Korea (NRF) grant funded by the Korea government (MSIP) (No. 2016R1E1A1A01942362).

Appendix 1. Comparison of double peaks between simulation and experiment

Comparison of depth and width of double peaks between simulation and experiment is given in Fig. 13. As mentioned in previous section, double peaks are observed only in hard sphere systems. Simulation was performed by using the potential-free method which describes hard sphere (Fig. 4). $\Gamma/\Gamma_{freezing}$ was set to 0.61 for simulation. Experimental data ware adopted from Fig. 9b and c of Nam et al. (2011) who used hard sphere systems. Volume fraction was 0.514 in experiments. In Nam's paper, elastic and viscous stress were plotted at two γ_0 (0.7 and 4) which clearly shows existence of double peaks.

For depth, the experimental data are larger than those of simulation. However for width, the experimental data are very close to the prediction of simulation. Larger value of depth in experiment seems to be originated from a steep decrement in total stress near the flow reversal (Fig. 9a of Nam et al.). But this steep decrement is not observed in the simulation, in which hydrodynamic interactions is not considered properly. BD simulation provides only a qualitative description of the system.

Depth increases and width decreases in experiments as γ_0 changes from 0.7 to 4. However, direct comparison of depth and width as a function of γ_0 could not be conducted due to the lack of experimental data. They increase followed by a decrease in simulation as γ_0 increases, but these characteristics could not be completely matched with experiment.

Appendix 2. Effect of volume fraction on double peaks and excess entropy

The depth and width at different $\Gamma/\Gamma_{freezing}$ are given in Fig. 14 and the difference in the maximum and minimum of excess entropy is plotted in Fig. 15. All data were obtained by using the potential-free method. De = 80, and $\Gamma/\Gamma_{freezing}$ = 0.61, 0.71 and 0.81.

As $\Gamma/\Gamma_{freezing}$ increases, both depth and width decrease, and the γ_0 range where double peaks appear decreases. The difference in excess entropy decreases too and it affects the γ_0 range of double peaks as well as its depth. The effect of $\Gamma/\Gamma_{freezing}$ also supports that double peaks are observed in systems when the structural difference between the maximum- and minimum-ordered states is large.

References

Agrawal R, Kofke DA (1995) Thermodynamic and structural properties of model systems at solid-fluid coexistence I. Fcc and bcc soft spheres. Mol Phys 85(1):23–42. https://doi.org/10.1080/00268979500100911

Brańka AC, Heyes DM (2006) Thermodynamic properties of inverse power fluids. Phys Rev E – Statistical Nonlinear Soft Matter Phys 74:1–11

Besseling TH, Hermes M, Fortini A, Dijkstra M, Imhof A, van Blaaderen A (2012) Oscillatory shear-induced 3D crystalline order in colloidal hard-sphere fluids. Soft Matter 8(26):6931–6939. https://doi.org/10.1039/c2sm07156h

Cho KS, Hyun K, Ahn KH, Lee SJ (2005) A geometrical interpretation of large amplitude oscillatory shear response. J Rheol 49(3):747–758. https://doi.org/10.1122/1.1895801

Ding Y, Mittal J (2015) Equilibrium and nonequilibrium dynamics of soft sphere fluids. Soft Matter 11(26):5274–5281. https://doi.org/10.1039/C5SM00637F

Dzugutov M (1996) A universal scaling law for atomic diffusion in condensed matter. Nat 381(6578):137–139. https://doi.org/10.1038/381137a0

Ewoldt RH, Hosoi AE, McKinley GH (2008) New measures for characterizing nonlinear viscoelasticity in large amplitude oscillatory shear. J Rheol 52(6):1427–1458. https://doi.org/10.1122/1.2970095

Foss DR, Brady JF (2000a) Brownian dynamics simulation of hard-sphere colloidal dispersions. J Rheol 44(3):629–651. https://doi.org/10.1122/1.551104

Foss DR, Brady JF (2000b) Structure, diffusion and rheology of Brownian suspensions by Stokesian dynamics simulation. J Fluid Mech 407:167–200. https://doi.org/10.1017/S0022112099007557

Fuchs M, Ballauff M (2005) Flow curves of dense colloidal dispersions: schematic model analysis of the shear-dependent viscosity near the colloidal glass transition. J Chem Phys 122:1–6

Grand AL, Petekidis G (2008) Effects of particle softness on the rheology and yielding of colloidal glasses. Rheol Acta 47(5-6):579–590. https://doi.org/10.1007/s00397-007-0254-z

Gompper G, Ihle T, Kroll DM, Winkler RG (2009) Multi-particle collision dynamics: a particle-based mesoscale simulation approach to the hydrodynamics of complex fluids. Adv Polym Sci 221:1–87

Goudoulas TB, Germann N (2017) Phase transition kinetics and rheology of gelatin-alginate mixtures. Food Hydrocoll 66:49–60. https://doi.org/10.1016/j.foodhyd.2016.12.018

Hanley HJM, Rainwater JC, Hess S (1987) Shear-induced angular dependence of the liquid pair correlation function. Phys Rev A 36(4):1795–1802. https://doi.org/10.1103/PhysRevA.36.1795

Heyes DM, Brańka AC (2005) Mechanical, rheological and transport properties of soft particle fluids. Mol Simul 31:945–959

Heyes DM, Brańka AC (2008) Self-diffusion coefficients and shear viscosity of inverse power fluids: from hard- to soft-spheres. Phys Chem Chem Phys 10:4036–4044

Heyes DM, Melrose JR (1993) Brownian dynamics simulations of model hard-sphere suspensions. J Non-Newton Fluid Mech 46:1–28

Huang G, Zhang H, Liu Y, Chang H, Zhang H, Song H, Xu D, Shi T (2017) Strain hardening behavior of poly(vinyl alcohol)/borate hydrogels. Macromolecules 50(5):2124–2135. https://doi.org/10.1021/acs.macromol.6b02393

Hyun K, Wilhelm M (2009) Establishing a new mechanical nonlinear coefficient Q from FT-rheology: first investigation of entangled linear and comb polymer model systems. Macromolecules 42(1):411–422. https://doi.org/10.1021/ma8017266

Hyun K, Wilhelm M, Klein CO, Cho KS, Nam JG, Ahn KH, Lee SJ, Ewoldt RH, McKinley GH (2011) A review of nonlinear oscillatory shear tests: analysis and application of large amplitude oscillatory shear (LAOS). Prog Polym Sci (Oxf) 36(12):1697–1753. https://doi.org/10.1016/j.progpolymsci.2011.02.002

Khandavalli S, Hendricks J, Clasen C, Rothstein JP (2016) A comparison of linear and branched wormlike micelles using large amplitude oscillatory shear and orthogonal superposition rheology. J Rheol 60(6):1331–1346. https://doi.org/10.1122/1.4965435

Klein CO, Spiess HW, Calin A, Balan C, Wilhelm M (2007) Separation of the nonlinear oscillatory response into a superposition of linear, strain hardening, strain softening, and wall slip response. Macromolecules 40(12):4250–4259. https://doi.org/10.1021/ma062441u

Koumakis N, Brady JF, Petekidis G (2013) Complex oscillatory yielding of model hard-sphere glasses. Phys Rev Lett 110:1–5

Koumakis N, Brady JF, Petekidis G (2016) Amorphous and ordered states of concentrated hard spheres under oscillatory shear. J Non-Newton Fluid Mech 233:119–132

Koumakis N, Pamvouxoglou A, Poulos AS, Petekidis G (2012) Direct comparison of the rheology of model hard and soft particle glasses. Soft Matter 8(15):4271–4284. https://doi.org/10.1039/c2sm07113d

Lange E, Caballero JB, Puertas AM, Fuchs M (2009) Comparison of structure and transport properties of concentrated hard and soft sphere fluids. J Chem Phys 130:1–8

Lee J, Sung S, Kim Y, Park JD, Ahn KH (2017) A new paradigm of materials processing-heterogeneity control. Curr Opin Chem Eng 16:16–22. https://doi.org/10.1016/j.coche.2017.04.002

Lee YK, Nam J, Hyun K, Ahn KH, Lee SJ (2015) Rheology and microstructure of non-Brownian suspensions in the liquid and crystal coexistence region: strain stiffening in large amplitude oscillatory shear. Soft Matter 11(20):4061–4074. https://doi.org/10.1039/C5SM00180C

Lees AW, Edwards SF (1972) The computer study of transport processes under extreme conditions. J Phys C: Solid State Phys 5(15):1921–1928. https://doi.org/10.1088/0022-3719/5/15/006

Lin NYC, Goyal S, Cheng X, Zia RN, Escobedo FA, Cohen I (2013) Far-from-equilibrium sheared colloidal liquids: disentangling relaxation, advection, and shear-induced diffusion. Phys Rev E – Statistical Nonlinear Soft Matter Phys 88:1–10

Mason TG, Lacasse M-D, Grest GS, Levine D, Bibette J, Weitz DA (1997) Osmotic pressure and viscoelastic shear moduli of concentrated emulsions. Phys Rev E – Statistical Phys Plasmas Fluids Relat Interdiscip TOP 56:3150–3166

McMullan JM, Wagner NJ (2009) Directed self-assembly of suspensions by large amplitude oscillatory shear flow. J Rheol 53(3):575–588. https://doi.org/10.1122/1.3088848

Mohan L, Pellet C, Cloitre M, Bonnecaze R (2013) Local mobility and microstructure in periodically sheared soft particle glasses and their connection to macroscopic rheology. J Rheol 57(3):1023–1046. https://doi.org/10.1122/1.4802631

Nam JG, Ahn KH, Lee SJ, Hyun K (2011) Strain stiffening of non-colloidal hard sphere suspensions dispersed in Newtonian fluid near liquid-and-crystal coexistence region. Rheol Acta 50(11-12):925–936. https://doi.org/10.1007/s00397-011-0533-6

Nazockdast E, Morris JF (2012) Effect of repulsive interactions on structure and rheology of sheared colloidal dispersions. Soft Matter 8(15):4223–4234. https://doi.org/10.1039/c2sm07187h

Mitchell PJ, Heyes DM, Melrose JR (1995) Brownian-dynamics simulations of model stabilized colloidal dispersions under shear. J Chem Soc Faraday Trans 91(13):1975–1989. https://doi.org/10.1039/ft9959101975

Park JD, Ahn KH, Lee SJ (2015) Structural change and dynamics of colloidal gels under oscillatory shear flow. Soft Matter 11(48): 9262–9272. https://doi.org/10.1039/C5SM01651G

Park JD, Myung JS, Ahn KH (2016) A review on particle dynamics simulation techniques for colloidal dispersions: methods and applications. Korean J Chem Eng 33(11):3069–3078. https://doi.org/10.1007/s11814-016-0229-9

Pellet C, Cloitre M (2016) The glass and jamming transitions of soft polyelectrolyte microgel suspensions. Soft Matter 12(16):3710–3720. https://doi.org/10.1039/C5SM03001C

Petekidis G, Vlassopoulos D, Pusey PN (2003) Yielding and flow of colloidal glasses. Faraday Discuss 123:287–302. https://doi.org/10.1039/b207343a

Pieprzyk S, Heyes DM, Brańka AC (2014) Thermodynamic properties and entropy scaling law for diffusivity in soft spheres. Phys Rev E – Statistical Nonlinear Soft Matter Phys 90:1–16

Poulos AS, Renou F, Jacob AR, Koumakis N, Petekidis G (2015) Large amplitude oscillatory shear (LAOS) in model colloidal suspensions and glasses: frequency dependence. Rheol Acta 54(8):715–724. https://doi.org/10.1007/s00397-015-0865-8

Salehiyan R, Song HY, Hyun K (2015) Nonlinear behavior of PP/PS blends with and without clay under large amplitude oscillatory shear (LAOS) flow. Korea Aust Rheol J 27(2):95–103. https://doi.org/10.1007/s13367-015-0010-3

Siebenburger M, Fuchs M, Winter H, Ballauff M (2009) Viscoelasticity and shear flow of concentrated, noncrystallizing colloidal suspensions: comparison with mode-coupling theory. J Rheol 53(3):707–726. https://doi.org/10.1122/1.3093088

Senff H, Richtering W (1999) Rheology of a temperature sensitive core-shell latex. Langmuir 15(1):102–106. https://doi.org/10.1021/la980979q

Truskett TM, Torquato S, Debenedetti PG (2000) Towards a quantification of disorder in materials: distinguishing equilibrium and glassy sphere packings. Phys Rev E – Statistical Phys Plasmas Fluids Relat Interdiscip TOP 62:993–1001

Wang G, Swan JW (2016) Large amplitude oscillatory shear of hard-sphere colloidal dispersions: Brownian dynamics simulation and Fourier-transform rheology. J Rheol 60(6):1041–1053. https://doi.org/10.1122/1.4955433

Wilhelm M (2002) Fourier-transform rheology. Macromol Mater Eng 287(2):83–105. https://doi.org/10.1002/1439-2054(20020201)287:2<83::AID-MAME83>3.0.CO;2-B